Science Arts & Métiers (SAM)
is an open access repository that collects the work of Arts et Métiers Institute of Technology researchers and makes it freely available over the web where possible.

This is an author-deposited version published in: https://sam.ensam.eu
Handle ID: .http://hdl.handle.net/10985/18601

To cite this version :

Bassem BARKIA, Pascal AUBRY, Paul HAGHI-ASHTIANI, Thierry AUGER, Lionel GOSMAIN, Frédéric SCHUSTER, Hicham MASKROT - On the origin of the high tensile strength and ductility of additively manufactured 316L stainless steel: Multiscale investigation - Journal of Materials Science and Technology - Vol. 41, p.209-218 - 2020

Any correspondence concerning this service should be sent to the repository Administrator : scienceouverte@ensam.eu

On the origin of the high tensile strength and ductility of additively manufactured 316L stainless steel: Multiscale investigation

Bassem Barkia[a,*], Pascal Aubry[a], Paul Haghi-Ashtiani[b], Thierry Auger[c], Lionel Gosmain[a], Frédéric Schuster[d], Hicham Maskrot[a]

[a] DEN-Service d'Etudes Analytiques et de Réactivité des Surfaces, CEA, Université Paris-Saclay, 91191, France
[b] Laboratoire de Mécanique des Sols, Structures et Matériaux, Centralesupélec, UMR CNRS 8579, Université Paris-Saclay, 92295, France
[c] Arts et Métiers ParisTech, PIMM, UMR CNRS 8006, 75013 Paris, France
[d] CEA Cross-Cutting Program on Materials and Processes Skills, 91191, Gif-sur-Yvette, France

Keywords:
Additive manufacturing
Austenitic stainless steel
Dislocation structure
Twinning
Mechanical behavior
Anisotropy

A B S T R A C T

We report that 316L austenitic stainless steel fabricated by direct laser deposition (DLD), an additive manufacturing (AM) process, have a higher yield strength than that of conventional 316L while keeping high ductility. More interestingly, no clear anisotropy in tensile properties was observed between the building and the scanning direction of the 3D printed steel. Metallographic examination of the as-built parts shows a heterogeneous solidification cellular microstructure. Transmission electron microscopy observations coupled with Energy Dispersive X-ray Spectrometry (EDS) reveal the presence of chemical micro-segregation correlated with high dislocation density at cell boundaries as well as the in-situ formation of well-dispersed oxides and transition-metal-rich precipitates. The hierarchical heterogeneous microstructure in the AM parts induces excellent strength of the 316L stainless steel while the low staking fault energy of the as-built 316L promotes the occurrence of abundant deformation twinning, in the origin of the high ductility of the AM steel. Without additional post-process treatments, the AM 316L proves that it can be used as a structural material or component for repair in mechanical construction.

1. Introduction

Metal additive manufacturing (AM) has gained significant academic and industry interest as it provides the opportunity to made complex-shaped parts that can be used in several domains [1–3]. AM could revolutionize many industrial sectors by decreasing material waste, component lead-time and carbon footprint [4]. AM processes can be classified into two principal classes: Powder bed fusion based technologies (PBF), such as selective laser melting (SLM) [5] and direct laser deposition (DLD) [6], such as laser engineered net shaping (LENS), a promising additive technology that is currently being developed [7]. The DLD/LENS process can be used to produce near-net shaped components or treat damaged or worn areas of a component [8]. The DLD/LENS technology has proved to be effective to fabricate a wide range of materials including stainless steels, titanium, nickel-base super alloys and cobalt-base alloys, etc [9–12].

316L austenitic stainless steel, in particular, is considered as one of the most widely used materials today owing to its high corrosion and oxidation resistance and its excellent strength and ductility [13,14]. Its area of application is increasing continuously. Currently, austenitic steels are mainly manufactured using forging, casting and extrusion [15]. The final product obtained from these conventional techniques need to welded or machined into the final shape, which makes these technologies time consuming. In addition, the machining of austenitic steels is relatively expensive and welding may induce corrosion sensitive grain boundaries [15,16]. Thus, the austenitic stainless steel is particularly interesting for laser additive manufacturing.

The currently available literature show that a large number of previous studies were dedicated to the 3D printing of 316L, especially using SLM technique [17–21]. However, limited research has been carried out on 316L using LENS technology compared to SLM. Most of these studies were focused on the effect of process parameters or heat treatment on the microstructure and/or the mechanical properties of the LENS 316L [22–27]. The presence of build defects (e.g., porosity, lack of powder melting. . .) may contribute to poor mechanical properties (low elongation and/or low Young's modu-

* Corresponding author.
E-mail address: bassem.barkia@polytechnique.edu (B. Barkia).

Table 1
Chemical compositions of the as-received 316 L powder compared to the ASTM specifications for 316L (wt.%).

Element	C	Cr	Co	Mn	P	Ni	Si	S	Mo	V	Cu	Fe
Powder	0.016	17.7	0.15	0.29	0.010	12.6	0.58	0.026	2.33	0.026	0.024	Bal.
ASTM	0.03_{Max}	16-18	–	2.0_{Max}	0.045_{Max}	10-14	0.75_{Max}	0.03_{Max}	2–3	–	–	Bal.

lus) of the AM 316L parts [22–25]. Furthermore, the effect of the building direction on the mechanical performances of the LENS 316L was poorly studied and rarely related to its microstructure and/or the crystallographic texture [23,26,27]. Finally, very few studies have strived to quantify the as-built microstructure at fine scale [26] and the investigation on the deformation modes of the LENS-processed 316L is still lacking.

Therefore, in order to fill this gap, the aim of this study is to use the LENS technology to fabricate high-density parts of 316L with a combination of high strength and ductility (a particular interest will be granted to the effect of the building direction on microstructure and tensile properties). Fine scale TEM investigations of the microstructure before and after tensile testing have been performed to develop a better understanding on the non-equilibrium as-built microstructure and the deformation modes of the additively manufactured 316L. Based on these observations, a correlation between the microstructural features and the resulting tensile properties is proposed. Finally, mechanical results from the 3D printed 316L will be compared with that of conventionally processed 316L.

2. Experimental

2.1. Material & additive manufacturing processing

Gas atomized spherical 316L powder (supplied by ERASTEEL, Sweden) with particle size of 45–106 μm was used as starting material. The chemical composition of the as-received powder respects the recommendation limit of the ASTM standard values for 316L [28] (see Table 1).

The laser metal depositions were performed using a LENS MR-7 System (OPTOMEC, Inc. Albuquerque, NM, USA). The LENS machine consists of a 3 kW Yb-fiber laser; a coaxial powder feed system, a controlled environment glove box and a motion control system. To limit the material oxidation during deposition at high temperature, the chamber was purged with high purity argon in order to maintain the oxygen concentration below 10 ppm during processing. The LENS control software lets the operator set the process parameters such as laser power, powder flow rate or layer thickness.

Two rectangular bars of 70 mm × 30 mm × 30 mm and 30 mm × 30 mm × 70 mm dimensions were fabricated from the 316L powder as shown schematically in Fig. 1. The two parts were built on a 150 mm × 50 mm × 10 mm 316L stainless steel plates with process parameters reported in Table 2. Note that a bidirectional scanning strategy was adopted, i.e., during each layer, the main direction of the hatch pattern is tilted by 90°.

2.2. Microstructural & mechanical characterization

For microstructural analyzes, the lateral surface and the top surface refer to the surface parallel and perpendicular to the building direction, respectively, as shown in Fig. 1.

Optical microscopy (OM; ZEISS Axio Imager 2), scanning electron microscopy (SEM; JEOL JMS 7000 F; 15 kV) equipped with an electron backscatter diffraction (EBSD) detector were used to examine the microstructure and the crystallographic texture of the as-built 316L samples. At microscale, transmission electron microscopy observations and Energy Dispersive X-Ray Spectroscopy (EDS) characterization were carried out using a FEI TITAN^3 transmission electron microscope operating at 300 kV.

For phase identification, X-ray diffraction (XRD) analyzes of the as-received powder and the as-built parts were performed on a diffractometer (XRD, Brucker D8 ADVANCE) with copper radiation source under 40 kV voltage and 40 mA current. The XRD data were collected over an angular range of 40–120° using a step size of 0.02°.

For OM, SEM and XRD analyzes, the samples were first mechanically and then electrolytically polished in a 10% oxalic acid aqueous solution at 15 V for 20 s. For TEM observations, 3-mm disk were machined and mechanically ground to a thickness of 100 μm. Final thinning of the disk to electron transparency was performed using a Tenupol-5 twin jet polisher, in a solution of 10% perchloric acid and 90% acetic acid at room temperature and an operating voltage of 15 V.

To investigate the tensile properties of the as-built bars, longitudinal (tensile axis parallel to the building direction) and transverse (tensile axis perpendicular to the building direction) cylindrical specimens of 4 mm diameter and 15 mm gage length were machined from the AM parts (see Fig. 1). Uniaxial tensile tests were conducted at room temperature on an electromechanical testing frame (MTS 20/M, 100 kN load cell) at a cross-head speed of 2.5 μm/s. The yield strength $\sigma_{y,0.2\%}$ was evaluated by measuring the proof stress at 0.2% plastic strain.

3. Results and discussion

3.1. Density measurement and phase constitution

The density measurement results conducted by Archimedes method showed that a high density of >99.7% was achieved for the two fabricated parts (the density of conventional 316L steel was taken as a reference value). Moreover, the SEM examination of high-resolution micrographs does not show the presence of any pores or voids. These observations suggest that the difference in the measured density between the AM 316L and the conventional 316L cannot be attributed to the presence of voids but rather to the formation of inclusions, whose density is lower than that of the matrix, as will be shown later.

A comparison of the XRD patterns for the powder and the as-built 316 L samples is shown in Fig. 2. Both the as-milled powder and the deposited samples consist of pure face-centered-cubic (FCC) austenite phase. Indeed, the strongest lines of ferrite should appear at 44.7° and 65° [29] and, their absence in Fig. 2, indicates the fully austenitic structures of the analyzed samples. The theoretical line intensities for the austenite are 100%, 44% and 24% for the lines (111), (200) and (220), respectively [30]. These ratios were checked for the powder analysis but were not completely obeyed for the as-built 316L because of the crystallographic texture generated by the LENS process. Furthermore, compared to the as-received powder, the austenite peaks of the additively manufactured samples are slightly broader because of the presence of residual stresses and initial dislocations induced by the LENS process as will be discussed below.

3.2. General microstructure

Representative 3D optical view of the as-built microstructure is shown in Fig. 3(a). The material has a layered microstructure char-

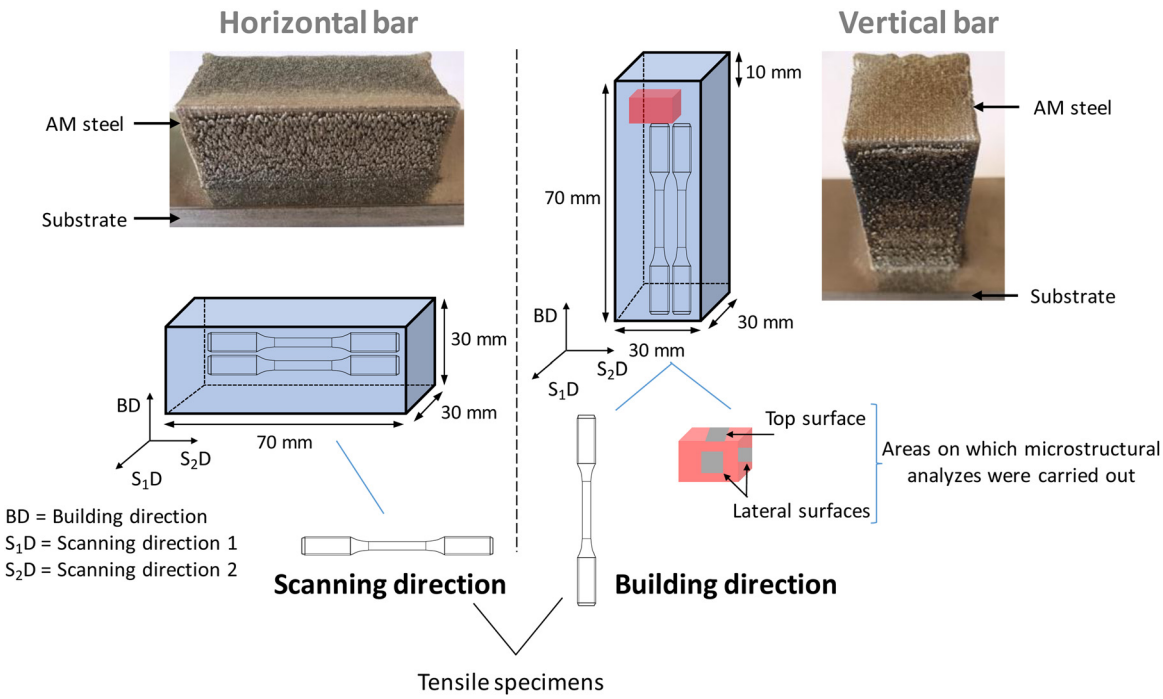

Fig. 1. Schematic of the horizontally and vertically built parts showing the positions from which tensile specimens were extracted and the areas on which microstructural analyzes were performed.

Table 2
Processing parameters used in directed laser deposition of the two additively manufactured parts.

Processing parameters	Laser power (W)	Travel speed (mm/s)	Layer thickness (mm)	Hatch spacing (mm)	Powder flow rate (g/min)
Vertical & horizontal bars	600	6.35	0.40	0.60	6

acterized by melt pools generated by the laser beam. The depth and the width of the melt pools are about 450 and 900 μm respectively. No evidence of cracks, pores or un-melted powder was observed. A closer 3D view of the microstructure is presented in Fig. 3(b) where EBSD image quality map (IQ) and grain color map showing grains in random colors were superimposed. The micrograph reveals that many grains include the melt-pool boundaries. This observation suggests an epitaxial growth of the grains from re-melted zones, following the maximum temperature gradient directions.

At higher magnification, high-resolution SEM micrographs revealed that the as-built parts are characterized by a typical cellular structure (Fig. 4). The cells are about 3–4 μm in diameter and a few tens of microns in length. The cellular structure is generally attributed to the high cooling speed that could reach 10^3–10^4 K/s during the LENS process as reported by Wang et al [31]. It is suggested that, with faster cooling rate; the solidification microstructure can evolve from planar to cellular to dendritic [32,33]. Cells are equiaxed or elongated, depending on their growth direction being strongly influenced by the direction of the thermal gradient (Fig. 4(c) and (d)). Moreover, elongated cells are especially observed along the melt-pool boundaries compared to more equiaxed ones in the center of the melt-pool. Furthermore, the high-resolution SEM image reported in Fig. 4(b) revealed the presence of spherical nano-inclusions with size ≤200 nm. Because of their small size, the SEM resolution was not enough to determine the chemical composition of the nano-inclusions. TEM observations are then conducted for further understanding of the fine microstructure induced by the LENS Process.

Fig. 5(a) and (b) shows inverse pole figure (IPF) maps relative to the building direction of the top surface (S_1D-S_2D) and the lateral surface (BD-S_1D) of the as-built 316L. The EBSD scans obtained from 1.3 mm × 1 mm areas were post-processed to evaluate the grain size by a standard metallographic technique using the intercept line method [34]. Grain boundaries were detected using grain detection angle of 5°. Although the grain size varied from about 20 to 350 μm, grains are quasi-equiaxed and the measured average grain size in the BD-S_2D as well as in the S_1D-S_2D plane is around 60 μm. Note that the achievement of equiaxed grains is desirable because high aspect ratio (grain morphology), often obtained in AM, can lead to an anisotropic plastic behavior of metallic materials: materials deform differently when being tested in different directions [35]. The plastic anisotropy could constitute a barrier to the application of advanced alloys [36]. It is obvious that the nearly equiaxed microstructure obtained in this study can be beneficial to the mechanical response and failure behavior of the AM steel, especially in the case of multi-axial deformation. For several set of parameters, Wang et al. [37] reported that the aspect ratio of the 304L SS made by DLD varied between 2 and 3.2. For the 316L obtained by LENS process, Yadollahi et al. [22] also observed elongated grains parallel to the building direction without quantifying the aspect ratio.

More than 90% of grain boundaries were of high angle types ($\theta \geq 15°$) with an average misorientation angle of about 32° in section along BD and 37° in the section perpendicular to BD. The misorientation across boundaries is an important microstructural parameter since it indicates the density of high angle grain boundaries (HAGB). HAGB provide obstacles to cleavage crack propagation [38,39] and thus enhance the fracture toughness. Few data in the literature are available concerning the grain boundary misorientation in austenitic steels fabricated by DLD/LENS technique. Yadollahi et al. [22] reported with their processing

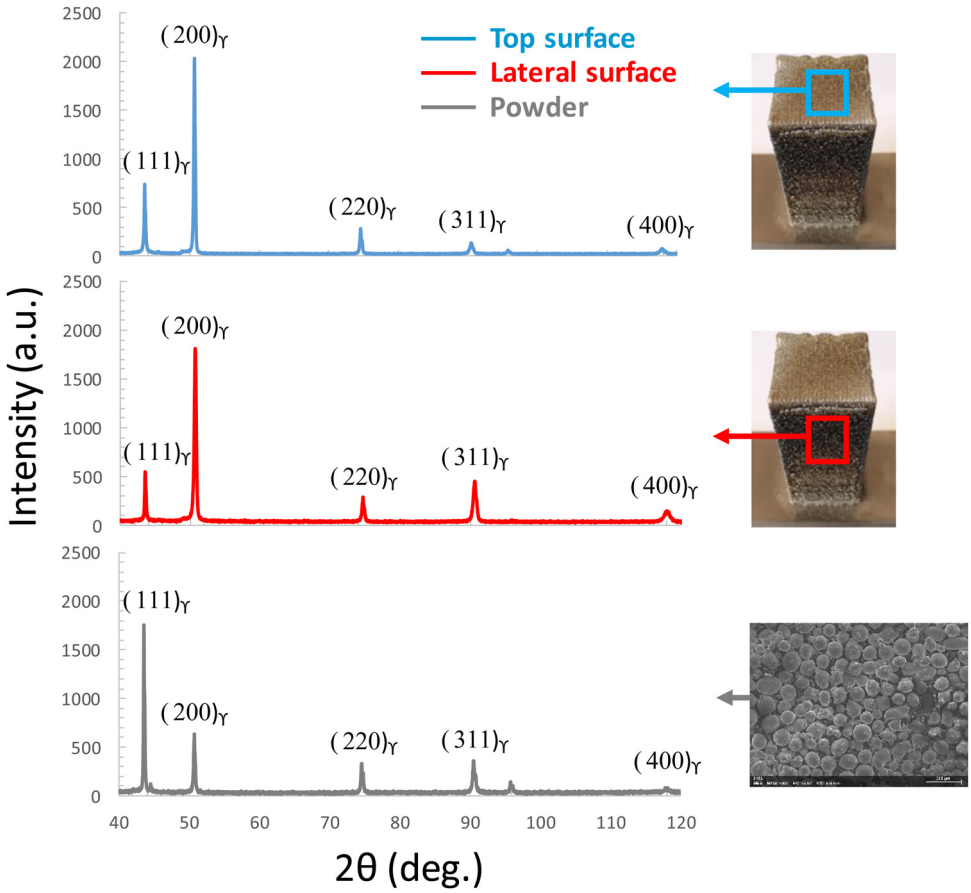

Fig. 2. The XRD patterns taken on the powder, the lateral and the top surface of the as-built 316L.

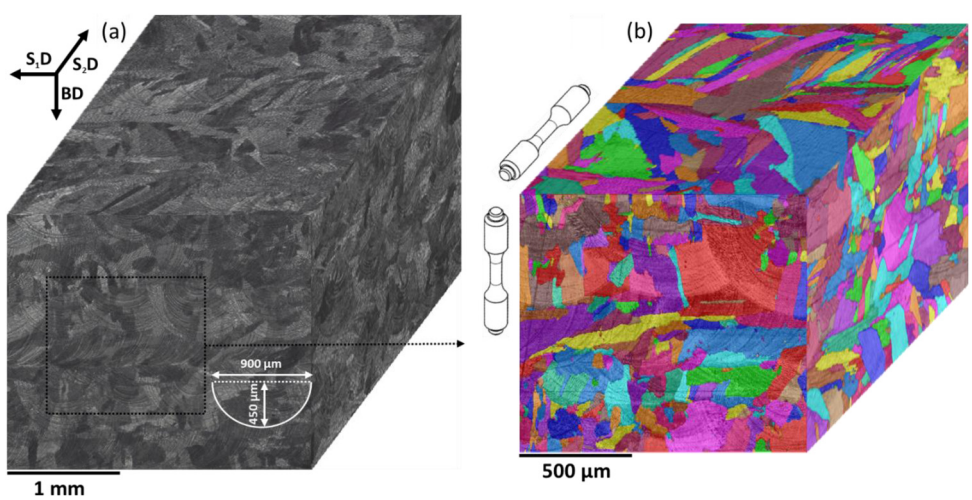

Fig. 3. 3D view of the as-built microstructure (a) optical micrograph; (b) Image quality (IQ) + color grain map.

parameters that the majority of grain boundaries has very low misorientation angles (1–4°) and that the average misorientation angles were about 14° in the as-built 316L and doesn't exceed 30° after heat treatment for 2 h at 1150 °C.

{100} and {110} pole figures calculated from the EBSD maps of the lateral surface (BD-S_2D plane) and the top surface (S_1D-S_2D plane) are shown in Fig. 5(c) and (d), respectively. In both cases, the pole figures show similar textures with the presence of a strong common (100) orientation aligned with the building direction BD and with the two scanning directions S_1D and S_2D (Maximum texture intensity of 3.6 times random). To our knowledge, such a kind of crystallographic texture has never been reported for austenitic steel made by DLD/LENS process. However, Kurzynowski et al. [20] observed the same kind of texture (i.e. strong {001} texture with respect to the building and scanning directions) in 316L made by selective laser melting (SLM). The samples were made at 200 W using the älternate-hatchs̈canning strategy (i.e., changing the scan direction by 90° between two successive layers). It is important to note that, in AM process, the texture evolution is affected by both the growth directions of the grains and the maximum heat flow directions. Thijs et al. [40] reported that the directional solidification and thus the resulting crystallographic texture would

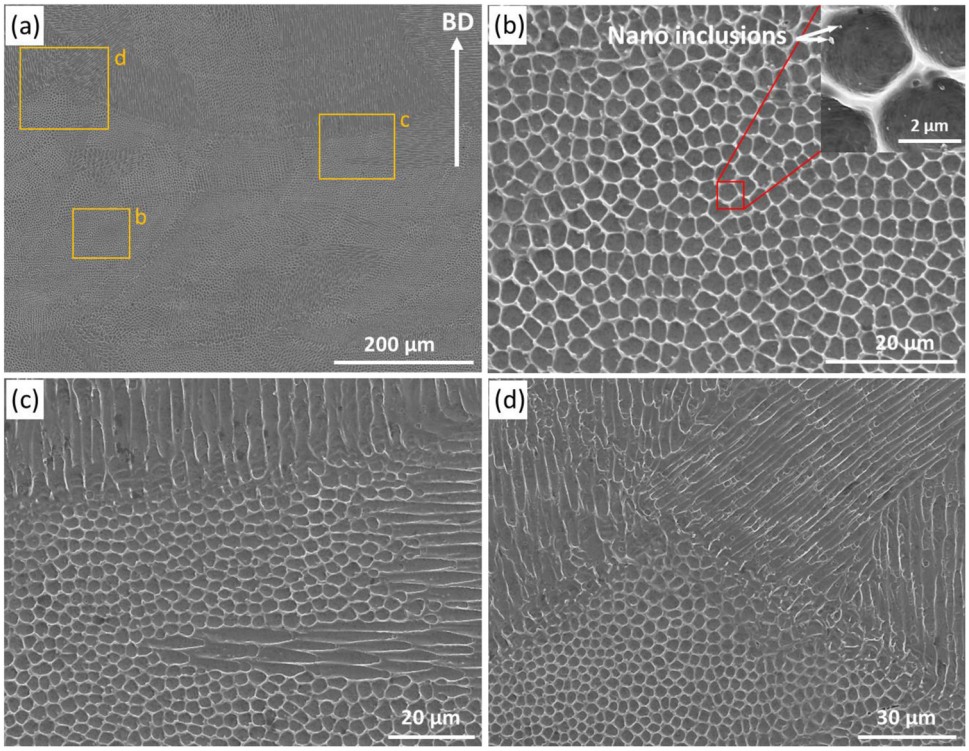

Fig. 4. SEM images illustrating the typical cellular microstructure at (a) low and (b–d) high magnification corresponding to the yellow areas indicated in Fig. 4(a); (b) equiaxed cells; (c,d) evidence of elongated cells at the melt pool boundaries.

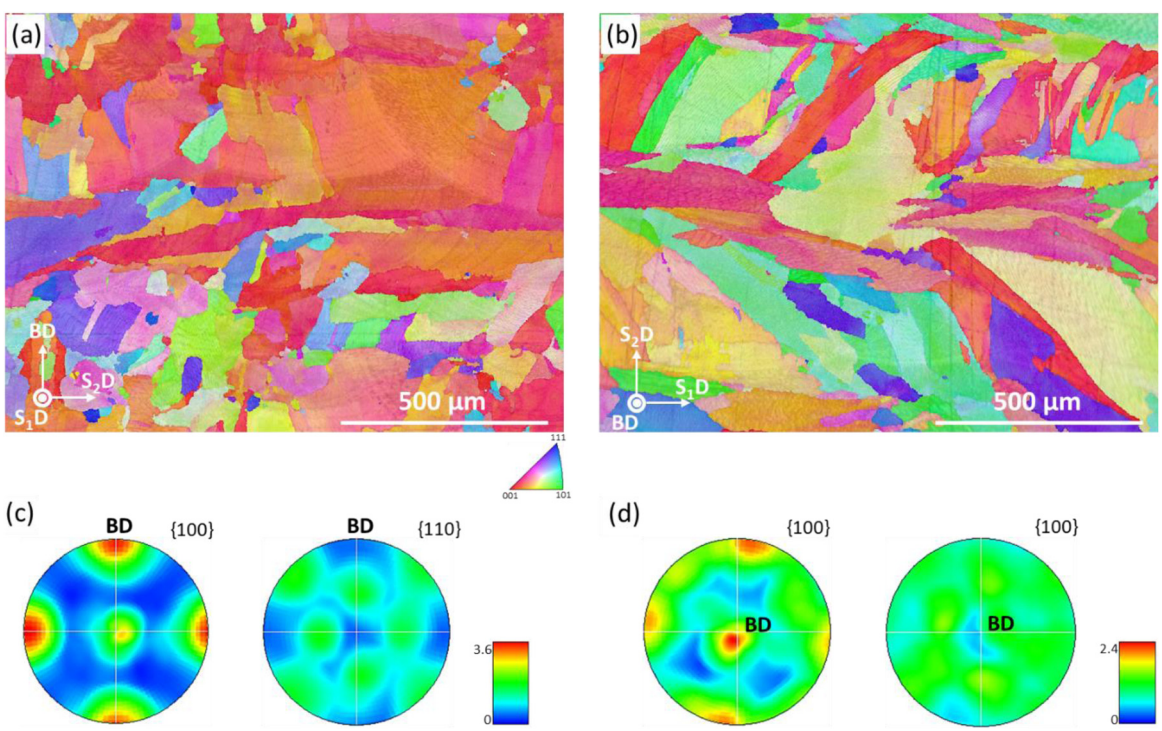

Fig. 5. Electron back-scattered diffraction (EBSD) inverse pole figure (IPF) relative to the building direction + IQ in (a) the lateral surface; (b) the top surface and (c,d) the corresponding pole figures.

depend on the adopted scanning strategy and building direction. The bidirectional scanning strategy used in this study is believed to be responsible for a reduction of the texture intensity along the building and scanning directions, which consequently reduces the anisotropy in the resulting mechanical properties.

3.3. Deep microstructure features

The TEM analyzes were performed on thin foils sectioned normal to the scanning direction S_1D. Fig. 6(a) shows representative bright field TEM micrographs of the initial microstructure of the

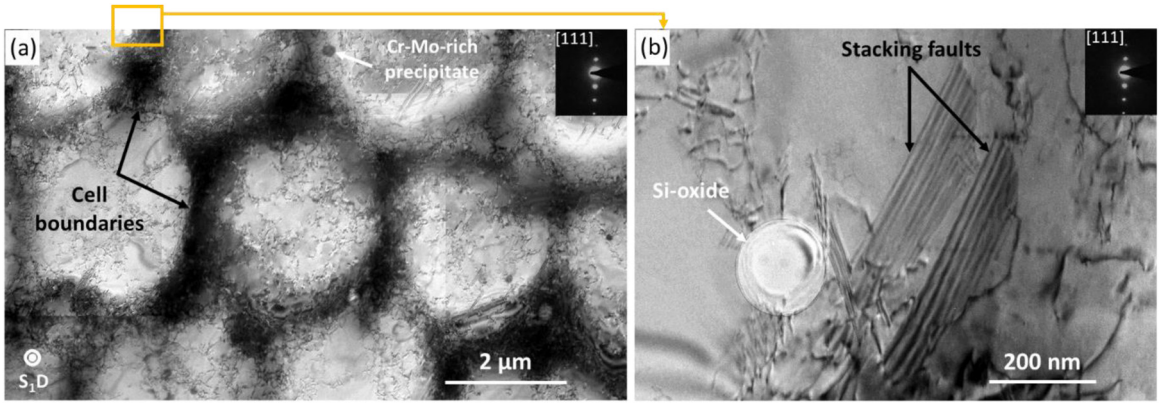

Fig. 6. TEM bright field micrographs of the typical microstructure of the as-built 316L: (a) cellular structure with arrays of dislocations pilling up at cell boundaries; (b) evidence of stacking faults and inclusions.

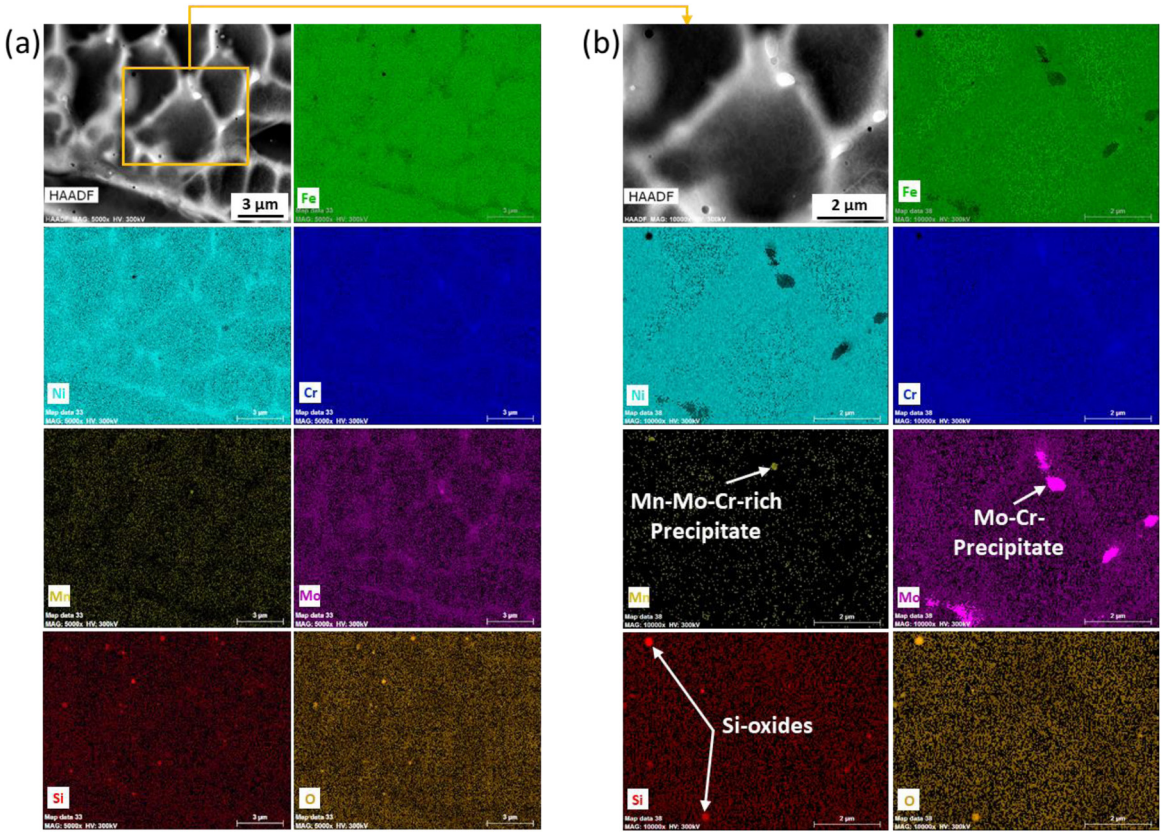

Fig. 7. (a) STEM-HAADF micrograph of the as-built 316L and the corresponding STEM-EDS chemical maps revealing segregation at cell boundaries; (b) evidence of Si-oxides and transition-metal-rich precipitates.

as-built 316L. The non-deformed material represent extensive network of dislocations at the cell boundaries. A closer view in the cell interiors revealed the presence of dislocation tangles and extended band of stacking faults as evidenced in Fig. 6(b). The dislocation cell structure formed in the AM steel is similar to the microstructure obtained under severe plastic deformation process. The thermal contraction induced by the rapid solidification is thought to be responsible for the high dislocation density in the AM parts [41].

Furthermore, the white contrast at the cell boundaries on the HAADF-STEM (Z contrast) image presented in Fig. 7(a) compared to the interior of the cells reveals an enrichment in heavier elements at the cell boundaries. This observation is supported by the corresponding STEM-EDS maps where segregation of Mo, Ni and Cr correlated with the dislocation structures can be observed (Fig. 7(a)). There is also an anti-correlation with Fe and Mn. It is notable that the dislocation substructures developed over the same length scale (3–4 µm) that the cell size revealed by the SEM micrographs. It indicates that the dislocation substructures are correlated with chemical micro-segregation.

The STEM-EDS maps in Fig. 7(b) revealed the presence of Si-containing oxides (from 50 to 200 nm in size) as well as transition-metal-rich precipitates, in which Mo, Mn and Cr content varies along the cell boundaries. These same particles (i.e. Si-oxides and Cr-Mo-rich precipitates) can also be observed in the TEM bright field micrographs shown in Fig. 6. Using the "Microprobe STEM" technique on the transmission electron microscope, the electron diffraction patterns (EDPs) corresponding to the two types of inclusions were examined. The EDP analysis proved that the Si-oxides

Table 3
Tensile properties of the as-built 316L in building and scanning directions.

	Yield strength (MPa)	Elongation to failure (%)
Building direction	378 ± 3	54.5 ± 1
Scanning direction	440 ± 5	51.5 ± 0.8

depleted of Fe are amorphous while the transition-metal-rich precipitates were crystalline. One can expect that the crystallographic structure (i.e., amorphous or crystalline) would have an impact on the deformability of the particles and on the dislocation-inclusions interaction when the material is deformed.

These oxide inclusions are generated by *in-situ* oxidation during the LENS process due to the presence of residual oxygen in the build chamber. It entails the possibility of using the build atmosphere for controlling the interstitial content of the 3D printed steels and for the in-situ formation of oxide-dispersed steels (ODS), as reported by Springer et al [42]. It is well established that introducing oxide particles inside a steel matrix will improve the high-temperature mechanical properties [43,44]. A fine dispersion of oxide particles can also improve the radiation tolerance of stainless steels [45,46]. The formation of nano-inclusions in the 316L during AM process was reported in previous work especially during sintering/melting process [26,47]. The inclusions were suggested to be silicate-containing chromium and manganese, which is confirmed by our TEM observations.

3.4. Mechanical properties and deformation mechanisms

Tensile tests were carried out on the as-built 316L at room temperature along the building and scanning directions. The engineering stress vs. engineering strain curves of the specimens are shown in Fig. 8. The results showed that the loading direction has slight effects on mechanical properties: it makes the 0.2% yield strength change from 378 ± 3 to 440 ± 5 MPa and total elongation from 54.5% ± 1% to 51. 5% ± 0.8% (Table 3). That is to say, regardless the loading direction, the LENS 316L produced here has good combination of strength and elongation compared to the conventional 316L (see Fig. 9). Indeed, tensile tests revealed that the AM 316 L stainless steel has higher tensile strength compared to the 316L stainless steel processed by the other conventional manufacturing process without sacrificing its ductility (Fig. 9) [22,25,48–52].

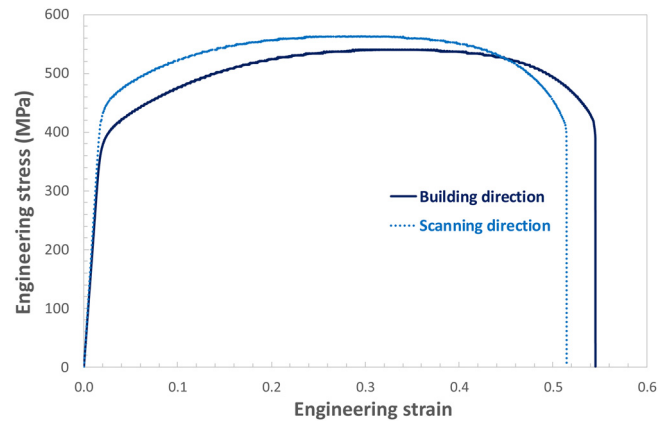

Fig. 8. Stress-strain curves of the as-built 316L strained at 2.5 μm s^{-1} at room temperature.

For comparison, the 0.2% yield stress of the as-built 316L is 440 ± 5 MPa compared with 170 MPa for the wrought 316L [48]. Moreover, the difference in yield strength between the building and scanning directions is only 62 MPa, which represents a small fraction of the observed difference between the strengths of the as-built 316L and the wrought 316L (more than 200 MPa). Previous studies on AM 316L showed that the DLD/LENS process improves the yield strength but reduces the ductility especially when the material is stressed along the building direction [25,26]. Compared to the results reported by Zhang et al. [25], the elongation to failure in the building direction obtained in the present study were far higher (54.5% in the present study against 21% in Ref. [25]). The poor elongation along the building direction reported by Zhang and Ziętala [25,26] is attributed to the presence of build defects (e.g. porosity and lack of fusion) among layer boundaries. It is evident that pre-existing dislocation structure contributes significantly to the high strength of the LENS 316L. The dislocation network as well as the chemical micro-segregation at cell boundaries formed during manufacturing hinder the dislocation motion resulting in higher yield strength compared to the conventional 316 L. Moreover, the nano-inclusions generated during the process will contribute to the increased strength of the AM 316L compared to as-cast or wrought material.

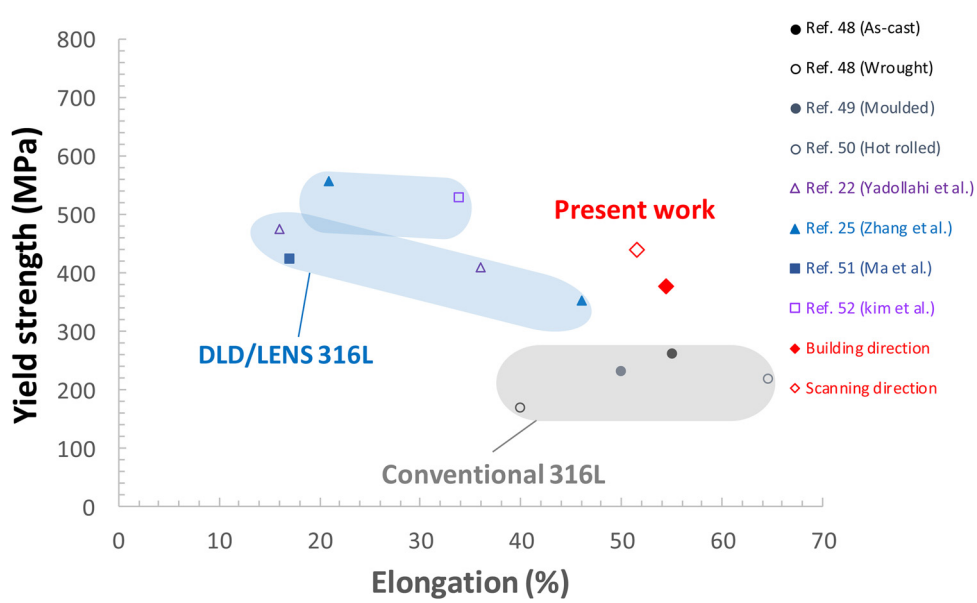

Fig. 9. The yield strength and ductility data of the DLD-LENS and conventional 316L SS from literature (the elongation to failure (elongation at break) was used).

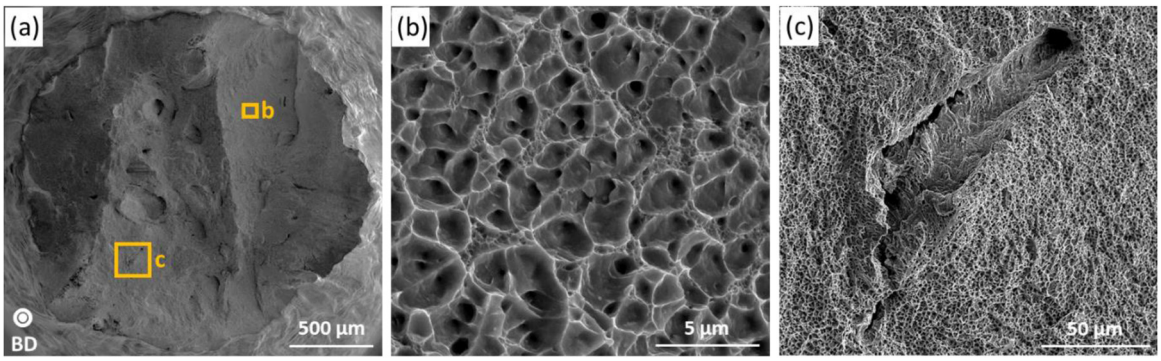

Fig. 10. SEM fractographs of the LENS 316L after tensile test along building direction (a) low magnification view; (b) typical ductile dimple fracture; (c) evidence of secondary cracking.

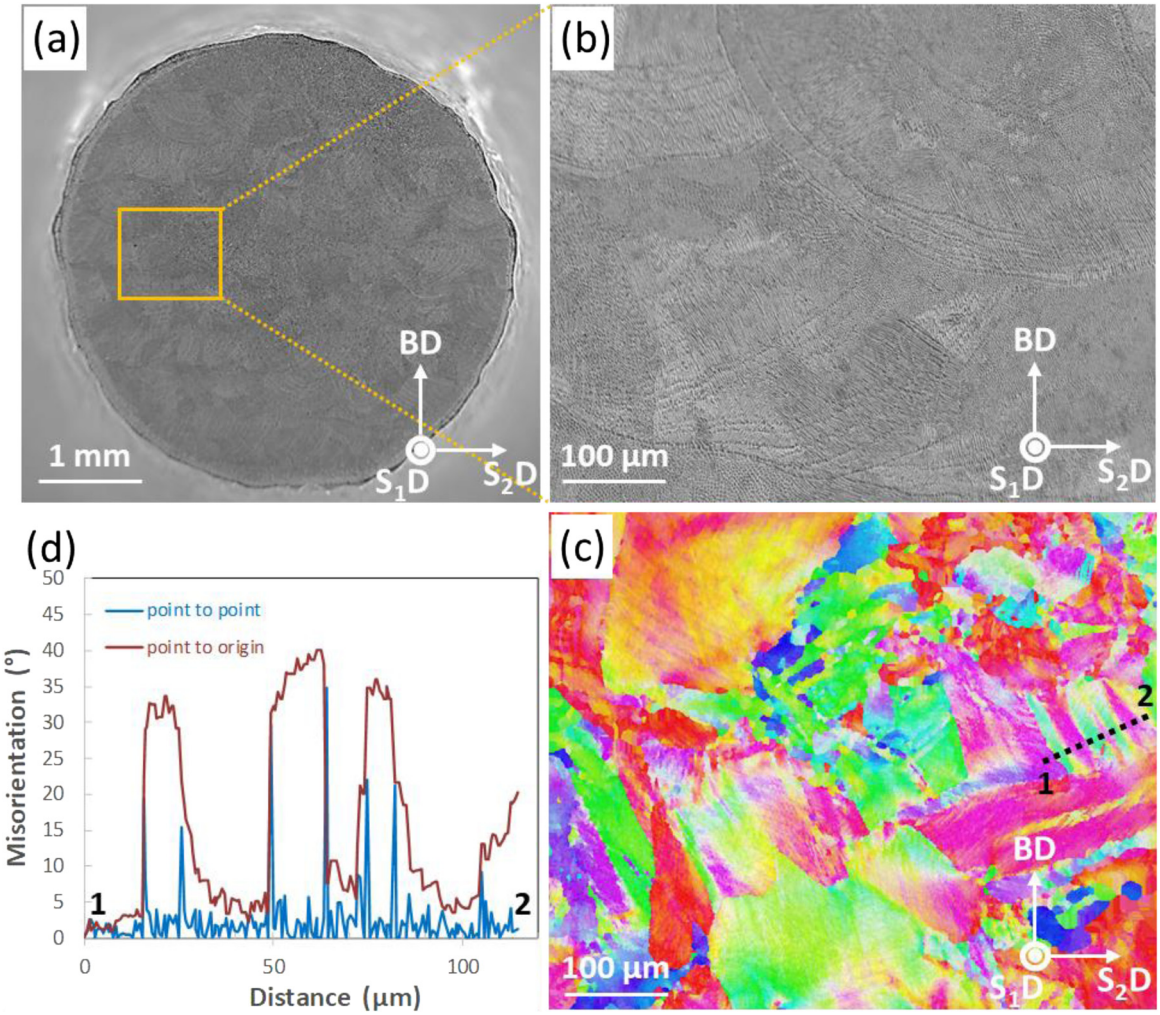

Fig. 11. (a) SEM micrograph of the cross section of the broken specimen; (b,c) SEM image of the area where EBSD analyzes were carried out with the corresponding IPF along the building direction + IQ; (d) misorientation profile along the black line in (c).

The fracture surface morphologies of the as-built 316L tested in building and scanning directions were analyzed. In both cases, typical ductile fracture features were observed although some evidence of brittle fracture was also visible. As shown in Fig. 10, ductile fracture via the void growth and coalescence mechanism was the dominant fracture mode. The dimples are a few microns in size, close to the typical cell dimensions of the as-built parts. Small dimples tend to increase the area of fracture surface so they absorb more deformation energy, thus improving the ductility by delaying the fracture process. Note that some secondary cracks, seemingly transgranular, were also observed. The formation and the propagation of secondary cracking is likely favored by the presence of nano-inclusions revealed in the as-built microstructure.

Despite the weakening effect (loss of ductility) that nano-inclusions could have on the 3D printed steel, the elongation to failure of the LENS 316L remains excellent. In order to investigate

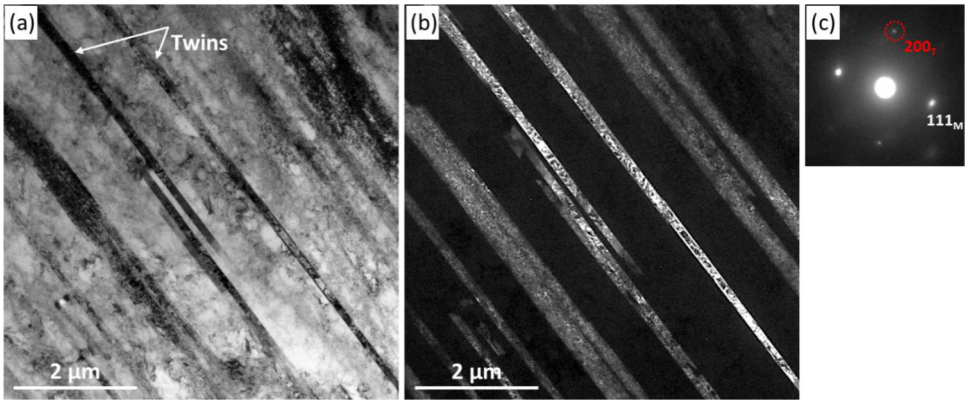

Fig. 12. (a) TEM bright-field micrograph revealing a high density of twins in the as-built sample strained to fracture; (b) the dark-field micrograph imaged using the diffraction spot outlined by the dashed circle in (c); (c) the corresponding electron diffraction pattern EDP (subscripts "T" and "M" refer to "Twin" and "Matrix" respectively).

the origin of such behavior, EBSD analysis and TEM observations were performed on the AM 316L strained to fracture to identify the activated deformation modes during plastic deformation.

Based on the IPF map analyzes in Fig. 11(c), the high lattice misorientation inside individual grains (10° to 15°) reflect the strong dislocation slip activity (slip-induced lattice reorientation mechanism). Furthermore, the examination of the SEM micrograph of the analyzed area (Fig. 11(b)) revealed distortion of the melt-pool boundaries, reflecting the intense strain at the melt-pool interfaces. More interestingly, compared to the initial microstructure of the non-deformed material, several deformation twins are observed in the IPF map confirming that twinning is mainly induced by deformation and suggesting that the contribution of mechanical twinning to plastic deformation is substantial. Twins were oriented parallel to one another and their thickness varies from few microns to several tens of microns. The misorientation plot across the matrix/twin interfaces showed that the mechanical twins were rotated by 30–40° relative to the matrix (Fig. 11(d)). Moreover, the phase map (not shown here) indicates that the deformed AM 316L has retained its austenitic phase against martensitic phase transformation. Conventional 316L undergoes strain-induced martensite transformation during plastic deformation as observed by Zhang et al. [53]. However, the EBSD analysis showed that the AM 316L did not transform during tensile test, suggesting that the mechanical stability of austenite is higher than that of conventional 316L. In a recent study conducted on a medium Mn austenitic steel, He et al. [54] showed that introducing initial dislocations by using a warm rolling process tend to stabilize the austenitic phase during plastic deformation at room temperature. One can assume that the dislocation cell structure formed in the as-built 316L tend to stabilize the austenitic phase of the AM steel and thus inhibit the strain-induced martensite transformation. Moreover, It is well established that the austenite stability is strongly related to the chemical composition (especially carbon and manganese) [55] but also to grain size [56]. Naghizadeh et al. [56] showed that below average grain size of ≈50 μm, the tendency to martensitic transformation diminishes by decreasing grain size. Thus, in addition to the initial dense dislocations, the fine cellular microstructure of the as-built 316L (cell size of 3–4 μm) would also contribute to the mechanical stability of austenite during plastic deformation.

The strong twinning activity was confirmed by TEM analyzes performed on the specimen strained to fracture. The TEM micrographs shown in Fig. 12 revealed the extensive activity of mechanical twinning. Dark field (DF) imaging has been used to unambiguously identify the observed micro-twins by selecting the appropriate diffraction spot. This strong tendency towards twinning is often observed in TWIP (Twinning Induced Plasticity) steels containing high content of Mn typically higher than 15 at.%, depending on the carbon content [57].

The propensity for mechanical twinning of the as-built 316L can be related to the value of the stacking fault energy (SFE). As the SFE decreases, the stacking faults become wider and the dislocation cross-slip mechanism more difficult thus promoting the deformation twinning [58]. From TEM observations of the AM 316L (see Fig. 6), extended band of stacking faults were observed suggesting that the non-deformed material has relatively low value of SFE, since the SFE is a measure the tendency for forming local stacking faults. Moreover, it is well known that a low value of SFE promotes mechanical twinning at the expense of dislocation glide [59] and that twinning induces large plasticity during deformation [60]. Thus, the pre-existing stacking faults in the non-deformed 316L favor mechanical twinning and improve the ductility of the AM 316L. Together with high density of initial dislocations, the mechanical twins contribute also to the high strength of the AM 316L steel since twin boundaries can act as obstacles to the dislocation glide by reducing the mean free path of dislocations during plastic deformation [61,62]. The spacing between deformation micro-twins can be less than a few hundred of nanometers (Fig. 12) that is narrower than the cell size of the as-built 316L (3–4 μm). It means that the influence of twinning on restricting the movement of dislocations is not negligible and would contribute to further improving the tensile strength of the AM 316L.

4. Conclusion

High strength and ductility 316L stainless steel samples were successfully printed in controlled atmosphere using LENS technique. Microstructural observations up to nanoscale revealed micro-cellular structure enriched with oxide particles and transition-metal-rich precipitates. The as-built components showed promising results regarding their structural integrity and resulting mechanical performances. In contrast to conventional counterparts where microstructure is homogenous, the hierarchical heterogeneous microstructures in the LENS parts induced excellent strength of 316L stainless steel. The strong deformation twinning induces large plasticity leading to high tensile ductility despite the formation of nano-inclusions in the AM steel. Furthermore, the build orientation seemed to have little to no effect on the mechanical properties of the as-built 316L. This study contributes to the understanding of the relationships between the LENS processing, microstructures, and resulting mechanical performances of 316 L stainless steel, key to satisfy the demands for new applications.

Acknowledgements

This work was supported financially by the French Alternative Energies and Atomic Energy Commission. The TEM observations were carried out using the equipment of the MATMECA consortium partially funded by the ANR under contract number (No. ANR-10-EQUIPEX-37).

References

[1] T. Debroy, H.L. Wei, J.S. Zuback, T. Mukherjee, J. Elmer, J.O. Milewski, A.M. Beese, A. Wilson Heid, A. De, W. Zhang, Prog. Mater. Sci. 92 (2018) 112–224.
[2] Y. Huang, M.C. Leu, J. Mazumder, A. Donmez, J. Manuf. Sci. Eng. 137 (2015) 014001–014010.
[3] W.J. Sames, F.A. List, S. Pannala, R.R. DeHoff, S.S. Babu, Int. Mater. Rev. 61 (2016) 315–360.
[4] E. Herderick, Additive Manufacturing of Metals: A Review, in: Materials Science and Technology, MS&T), Columbus, Ohio, 2011, pp. 1413–1427, October 16–20.
[5] G. Tapia, A. Elwany, J. Manuf. Sci. Eng. 23 (2014) 1917–1928.
[6] L. Bian, S.M. Thompson, N. Shamsaei, JOM 67 (2015) 629–638.
[7] E. Santos, M. Shiomi, Int. J. Mach. Tools Manuf. 46 (2006) 1459–1468.
[8] K.S. Prakash, T. Nancharaih, V.V.S. Rao, Mater. Today Proc. 5 (2018) 3873–3882.
[9] Z.E. Tan, J.H.L. Pang, J. Kaminski, H. Pepin, Addit. Manuf. 25 (2019) 286–296.
[10] J. Wang, J. Lu, X. You, R. Ullah, L. Sang, L. Chang, Y. Zhang, Z. Zhang, Mater. Sci. Eng. A 749 (2019) 48–55.
[11] K. Yuan, W. Guo, P. Li, J. Wang, Y. Su, X. Lin, Y. Li, Mater. Sci. Eng. A 721 (2018) 215–225.
[12] Y. Xiong, J.E. Smugeresky, L. Ajdelsztajn, J.M. Schoenung, Mater. Sci. Eng. A 493 (2008) 261–266.
[13] C.J. Novak, D. Peckner, in: I.M. Bernstein (Ed.), Handbook of Stainless Steels, McGraw-Hill, New York, 1977, pp. 1–4.
[14] Steels Atlas, Handbook for Stainless Steels, Technical Department (July) Atlas Steels Tech., 2010.
[15] R.W.K. Honeycombe, Bhadeshia HKDH Steels – Microstructure and Properties, 2nd ed., Edward Arnold, London, 1995.
[16] J. Xin, Y. Song, C. Fang, J. Wei, C. Huang, S. Wang, Fusion Eng. Des. 133 (2018) 70–76.
[17] U.S. Bertoli, B.E. MacDonald, J.M. Schoenung, Mater. Sci. Eng. A 739 (2019) 109–117.
[18] Z. Sun, X. Tan, S. Tor, C.K. Chua, NPG Asia Mater. 10 (2018) 127–136.
[19] H. Alsalla, C. Smith, L. Hao, Rapid Prototyp. J. 24 (2018) 9–17.
[20] T. Kurzynowski, K. Gruber, W. Stopyra, B. Kuźnicka, E. Chlebus, Mater. Sci. Eng. A 718 (2018) 64–73.
[21] M.L. Montero-Sistiaga, M. Godino-Martinez, K. Boschmans, J.P. Kruth, J. Van Humbeeck, K. Vanmeensel, Addit. Manuf. 23 (2018) 402–410.
[22] A. Yadollahi, N. Shamsaei, S.M. Thompson, D.W. Seely, Mater. Sci. Eng. A 644 (2015) 171–183.
[23] P. Guo, B. Zou, C. Huang, H. Gao, J. Mater. Process. Technol. 240 (2017) 12–22.
[24] M.S.F. de Lima, S. Sankaré, Mater. Des. 55 (2014) 526–532.
[25] Z. Zhang, S. Wang, W. Liu, X. Shang, Mater. Des. 55 (2014) 104–119.
[26] M. Ziętala, T. Durejko, M. Polański, I. Kunce, T. Płociński, W. Zieliński, M. Łazińska, W. Stępniowski, T. Czujko, K.J. Kurzydłowski, Z. Bojar, Mater. Sci. Eng. A 677 (2016) 1–10.
[27] G.T. Gray III, V. Livescu, P.A. Rigg, C.P. Trujillo, C.M. Cady, S.R. Chen, J.S. Carpenter, T.J. Lienert, S.J. Fensin, Acta Mater. 138 (2017) 140–149.
[28] ASTM-A276-06, Standard Specification for Stainless Steel Bars and Shapes, ASTM International, 100 Barr Harbor Drive, West Conshohocken, PA 19428, USA, 2006.
[29] ICDD, International Centre for Diffraction Data, in: Powder Diffraction File Number 00-052-0512, 2011.
[30] C.J. Bechtoldt, An X-Ray Diffraction Method for Determining the Amount of Austenite in an Austenite-Ferrite Mixture, vol. 709, Nat. Bur. Stand. (U.S.), Tech. Note, 1972.
[31] L. Wang, S. Felicelli, Y. Gooroochurn, P.T. Wang, M.F. Horstemeyer, Mater. Sci. Eng. A 474 (2008) 148–156.
[32] J.N. DuPont, Fundamentals of Weld Solidification, ASM Int., Materials Park, 2011.
[33] J.F. Lancaster, Metallurgy of Welding, Elsevier, Amsterdam, 1999.
[34] E.E. Underwood, Metals Handbook, Vol. 8, 8th ed., ASM, Metals Park, OH, 1973, p. 37.
[35] U.F. Kocks, C.N. Tome, H.R. Wenk, Texture and Anisotropy: Preferred Orientations in Polycrystals and Their Effect on Materials Properties, University Press, Cambridge, Cambridge, 1998, p. 391.
[36] M.S. Pham, A. Creuziger, M. Iadicola, A.D. Rollett, J. Mech. Phys. Solids 99 (2017) 50–69.
[37] Z. Wang, T.A. Palmer, A.M. Beese, Acta Mater. 110 (2016) 226–235.
[38] J. Nohava, P. Hausild, M. Karlik, P. Bompard, Mater. Charact. 49 (2002) 211–217.
[39] A.-F. Gourgues, H.M. Flower, T.C. Lindley, Mater. Sci. Technol. 16 (2000) 26–40.
[40] L. Thijs, M.L. Sistiaga, R. Wauthle, J.P. Kruth, J. Humbeeck, Acta Mater. 61 (2013) 4657–4668.
[41] S. Gorsse, C. Hutchinson, M. Gouné, R. Banerjee, Sci. Technol. Adv. Mater. 18 (2017) 584–610.
[42] H. Springer, C. Baron, A. Szczepaniak, E.A. Jägle, M.B. Wilms, A. Weisheit, D. Raabe, Mater. Des. 111 (2016) 60–69.
[43] K.L. Murty, I. Charit, J. Nucl. Mater. 383 (2008) 189–195.
[44] A.F. Rowcliffe, S.J. Zinkle, J.F. Stubbins, D.J. Edwards, D.J. Alexander, J. Nucl. Mater. 258–263 (2008) 183–192.
[45] A. Ramar, N. Baluc, R. Schaublin, J. Nucl. Mater. 367–370 (2007) 217–221.
[46] S. Ukai, M. Fujiwara, J. Nucl. Mater. 307–311 (2002) 749–757.
[47] K. Saeidi, X. Gao, Y. Zhong, Z.J. Shen, Mater. Sci. Eng. A 625 (2015) 221–229.
[48] A.S.M. Metals Handbook, in: D. Benjamin, C.W. Kirkpatrick (Eds.), Properties and Selection: Stainless Steels, Tool Materials and Special-Purpose Metals, Metal Handbook, Vol. 3, ASM Int. Met. Park, 1980, pp. 113–121.
[49] J. Rawers, F. Croydon, R. Krabbe, N. Duttlinger, Powder Metall. 39 (1996) 125–129.
[50] R. Song, J. Xiang, D. Hou, J. Iron Steel Res. Int. 18 (2011) 53–59.
[51] M. Ma, Z. Wang, D. Wang, X. Zeng, Opt. Laser Technol. 45 (2013) 209–216.
[52] D.K. Kim, W. Woo, E.Y. Kim, S.H. Choi, J. Alloys Compd. 774 (2019) 896–907.
[53] S.Y. Zhang, E. Compagnon, B. Godin, A.M. Korsunsky, Mater. Today: Proc. 2S (2015) S251–S260.
[54] B.B. He, M. Wang, M.X. Huang, Metall. Mater. Trans. A 50 (2019) 2971–2977.
[55] Z.C. Li, H. Ding, R.D.K. Misra, Z.H. Cai, Mater. Sci. Eng. A 682 (2017) 211–219.
[56] M. Naghizadeh, H. Mirzadeh,Steel Res. Int. 90 (2019), 1900153.
[57] M. Naghizadeh, H. Mirzadeh, Int. J. Plast. 16 (2000) 1391–1409.
[58] D. Hull, D.J. Bacon, Introduction to Dislocations, 4th ed., Butterworth-Heinemann, London, 2001.
[59] J. Lu, Lars Hultman, E. Holmström, K.H. Antonsson, M. Grehk, W. Li, L. Vitos, A. Golpayegani, Acta Mater. 111 (2016) 39–46.
[60] J.W. Christian, S. Mahajan, Prog. Mater. Sci. 39 (1995) 1–157.
[61] Y.T. Zhu, X.Z. Liao, X.L. Wu, Prog. Mater. Sci. 57 (2012) 1–62.
[62] J. Li, Y. Cao, B. Gao, Y. Li, Y. Zhu, J. Mater. Sci. 53 (2018) 10442–10456.